From a non-magnet to a ferromagnet: Mn+ implantation into different TiO2 structures

O. Yıldırım, S. Cornelius, M. Butterling, W. Anwand, A. Wagner, A. Smekhova, J. Fiedler, R. Böttger, C. Bähtz, and K. Potzger

Articles you may be interested in
The local environment of cobalt in amorphous, polycrystalline and epitaxial anatase TiO2:Co films produced by cobalt ion implantation
J. Appl. Phys. **117**, 183901 (2015); 10.1063/1.4919702

Room temperature ferromagnetism in N-doped rutile TiO2 films
J. Appl. Phys. **109**, 07C302 (2011); 10.1063/1.3535427

Absence of ferromagnetism in single-phase wurtzite Zn 1 − x Mn x O polycrystalline thin films
J. Appl. Phys. **108**, 073922 (2010); 10.1063/1.3486017

Structures and magnetic properties of p -type Mn : TiO 2 dilute magnetic semiconductor thin films
J. Appl. Phys. **106**, 043913 (2009); 10.1063/1.3204493

Magnetic and transport properties of (Mn, Co)-codoped ZnO films prepared by radio-frequency magnetron cosputtering
J. Appl. Phys. **98**, 053908 (2005); 10.1063/1.2039279

From a non-magnet to a ferromagnet: Mn$^+$ implantation into different TiO$_2$ structures

O. Yıldırım,[1,2,a)] S. Cornelius,[1,3] M. Butterling,[4] W. Anwand,[4] A. Wagner,[4] A. Smekhova,[5,6]
J. Fiedler,[1] R. Böttger,[1] C. Bähtz,[1,7] and K. Potzger[1]

[1]*Helmholtz-Zentrum Dresden - Rossendorf, Institute of Ion Beam Physics and Materials Research,*
Bautzner Landstr. 400, 01328 Dresden, Germany
[2]*Technische Universität Dresden, D-01062 Dresden, Germany*
[3]*Department of Chemical Engineering, Materials for Energy Conversion and Storage,*
Delft University of Technology, Julianalaan 136, NL-2628BL Delft, The Netherlands
[4]*Helmholtz-Zentrum Dresden - Rossendorf, Institute of Radiation Physics, Bautzner Landstr. 400,*
01328 Dresden, Germany
[5]*Faculty of Physics, Lomonosov Moscow State University (MSU), 119991 Moscow, Russia*
[6]*Faculty of Physics and CENIDE, University of Duisburg-Essen, Lotharstr. 1, 47048 Duisburg, Germany*
[7]*Rossendorf Beamline, European Synchrotron Radiation Facility, F-38043 Grenoble, France*

We report effect of the initial structural order on the resulting magnetic properties of manganese implanted TiO$_2$ films. Different microstructures of as-grown TiO$_2$ films, namely, amorphous, polycrystalline anatase, and epitaxial anatase, have been implant-doped with Mn$^+$ up to a concentration of 5 at. %. We found that different initial structures lead to different defect and charge carrier concentrations and, as a result, strongly influence the magnetic properties upon implantation. Depending on the initial microstructure, paramagnetism, secondary phases related magnetic properties as well as ferromagnetism could be observed in the films. © 2015 AIP Publishing LLC.
[http://dx.doi.org/10.1063/1.4938069]

Until the discovery of room temperature ferromagnetism (FM) in TiO$_2$:Co (anatase),[1] studies on dilute magnetic semiconductors (DMS) were mostly focused on II–VI and III–V compounds. The aforementioned report broadened the research area of DMS to oxides and it has stimulated numerous follow-up studies. The simple experimental concept of doping TiO$_2$ with a few atomic percent of 3d metal cations is expected to yield substitutional dopant sites, which are separated by large distances, yet ferromagnetically ordered.[2] Such a ferromagnetic order, covering long-range distances, is inexplicable in terms of common super-exchange and double exchange, which consider only the first or second nearest-neighbour cation interactions.[3] Therefore, the discovery of dilute magnetic oxides (DMOs) also fueled a debate on the origin and the mechanism of the observed FM in such systems. The origin of the observed FM in DMOs can vary from magnetic contaminations,[4] secondary phases[5] to open-volume defects,[6–8] which are considered as extrinsic or unwanted sources of FM. On the other hand, if FM occurs due to coupling of dopant atoms residing on substitutional sites within the host lattice, it is considered to be an intrinsic effect. Consequently, identifying electronic and defect properties of the material along with the chemical environment of the dopant is of primary importance in order to understand the interplay between extrinsic and intrinsic origins of the magnetic properties. In this study, TiO$_2$ films with different defect properties have been prepared by adjusting their initial microstructure. Subsequently, Mn$^+$ implantation was performed in order to dope the TiO$_2$ films, and the effect of the

microstructure on the resulting magnetic properties has been investigated along with electric transport and defect properties.

TiO$_2$ films of 300 nm thickness were grown on SrTiO$_3$ (100) single crystals by means of DC magnetron sputtering. A high purity oxygen deficient ceramic TiO$_{2-x}$ target was sputtered at 120 W in Ar/O$_2$ atmosphere at a pressure of 0.7 Pa containing ∼0.4 vol. % of O$_2$. These conditions were found to yield near-stoichiometric films confirmed by the absence of optical absorption below the bandgap of 3.2(±0.1) eV, as determined by spectral photometry (not shown). Amorphous TiO$_2$ films were obtained by deposition on unheated substrates. Polycrystalline anatase TiO$_2$ structure was achieved by post-growth annealing of initially amorphous layers at 450 °C for 1 h in vacuum ($< 2 \times 10^{-5}$ Pa). Epitaxial anatase TiO$_2$, on the other hand, was obtained by direct deposition on substrates heated to 500 °C. For a homogeneous depth distribution of the Mn ions, as compared to the Gaussian-like depth distribution for implantations at a single energy, five different energy and ion fluence combinations, as determined by SRIM simulations,[9] have been applied[10] (see Ref. 11 for a similar ion implantation depth profile calculation). The maximum implantation depth was calculated to be around 150 nm. By keeping the maximum implantation depth around 150 nm, the interfacial mixing between the film and substrate, as well as doping of the substrate, is avoided. Moreover, having the implantation profile somewhat thinner than the actual film thickness also helps to avoid the formation of interfacial clusters.[12] The crystalline structure of both as-grown and implanted TiO$_2$ films was controlled by means of X-ray diffraction (XRD) measurements using Ni-filtered Cu-Kα radiation of a PANalytical Empyrean diffractometer. The local atomic

a)Author to whom correspondence should be addressed. Electronic mail: o.yildirim@hzdr.de

coordination of the implanted Mn dopant was investigated by X-ray absorption near-edge spectroscopy (XANES) at Mn K-edge. XANES measurements were performed in fluorescence mode using energy-resolved detector at the ROBL-MRH setup of the BM-20 beamline at the ESRF in Grenoble, France. All structural characterizations were performed at room temperature. The magnetic properties of the implanted films were investigated by a superconducting quantum interference device (SQUID, Quantum Design MPMS XL 7). Magnetometry was performed as function of temperature and magnetic field. For all samples, zero field cooled (ZFC) and field cooled (FC) thermomagnetic measurements have been carried out in an applied external magnetic field of 15 mT. The electrical transport properties of the films were characterized using a LakeShore HMS 9709 Hall measurement system in the temperature range of 20 K and 300 K and an applied external field range of 1 T with probe current of 1 mA. Ohmic contacts were employed by sputtering gold onto sample corners and attaching silver wires with silver glue on top of gold layers. The Hall effect measurements were carried out in van der Pauw geometry. Positron annihilation spectroscopy (PAS) was performed at the Slow Positron System of Rossendorf (SPONSOR).[13] The positron beam emitted from a ^{22}Na radioactive source was accelerated up to 30 keV for depth resolved Doppler broadening spectroscopy. The S parameter, characteristic of open volume defect concentration within the film,[14] is extracted from the Doppler broadening of the 511 keV photon peak originating from positron-electron annihilation in the sample.

XRD pattern analysis shows that all of the observed diffraction maxima of the polycrystalline and epitaxial films can be identified with the anatase phase of TiO_2 (not shown). Moreover, out-of-plane c-axis texture, i.e., $TiO_2(001)\|STO(100)$, for as-grown epitaxial film is confirmed by rocking curve measurements at the anatase (004) reflection (not shown). Upon Mn$^+$ implantation, rutile formation is observed both in initially polycrystalline anatase and epitaxial anatase films. Similar XRD patterns along with a detailed analysis on the structural deformation by considering the formation of rutile phases upon ion implantation is given elsewhere.[11] However, given the weak contribution of rutile related peaks to the total XRD pattern, the initial anatase structure has been mostly preserved after implantation. Apart from the rutile phases, no other known Mn related secondary phases could be detected by XRD.

The Mn$^+$-implanted polycrystalline and epitaxial TiO_2 films show n-type degenerate semiconducting behavior, i.e., the electron density is temperature independent with free electron concentrations of 1.54×10^{19} cm^{-3} and 6.21×10^{18} cm^{-3}, for the Mn$^+$-implanted polycrystalline and epitaxial films, respectively. The room temperature electron mobilities are ~ 2 cm^2/V^{-1}s^{-1} for polycrystalline and ~ 15 cm^2/V^{-1}s^{-1} for epitaxial TiO_2:Mn film, which are comparable to the reported values for Nb doped epitaxial anatase TiO_2 films.[15] In the case of amorphous films, the contact resistance was above the measurement limit (>20 GΩ cm). Additionally, no anomalous Hall effect (AHE) has been observed for any of the three Mn$^+$-implanted samples within the investigated temperature range.

Figure 1 depicts the S parameter dependence on the positron energy as obtained from the PAS measurements on as-grown (a) and Mn$^+$-implanted (b) TiO_2 films. The data shown provide some depth information, because the positron energy defines the implantation depth of positrons into the sample, which is then followed by diffusion until annihilation takes place. Since the film surface acts as a positron sink, the S parameter is high at lowest positron energies (region I). Positrons implanted at higher energies remain in the bulk of the film, resulting in a plateau of the S parameter that provides information about defect concentration within the film (region II). Moreover, owing to the positive charge of the positron, PAS measurements are only sensitive to negatively charged or neutral vacancy defects. The PAS measurements on as-grown TiO_2 films reveal that the concentration of these defects is highest in as-grown amorphous TiO_2 and decreases in polycrystalline and further in epitaxial TiO_2 (Fig. 1(a)). After the Mn$^+$ implantation this trend is preserved (Fig. 1(b)). The more pronounced plateau of the S parameter depth profile observed in Mn$^+$-implanted polycrystalline and epitaxial films as compared to their as-grown states may be attributed to an increased sub-surface defect concentration, leading to suppressed positron diffusion towards the surface.

Figure 2(a) shows the Mn K-edge XANES spectra of the Mn$^+$-implanted TiO_2 films. Post-edge region of each spectrum was normalized to unity. The positions of the Mn K-edges for all three TiO_2:Mn structures coincide with those of MnO[16] and MnTiO$_3$,[17] confirming that most of the
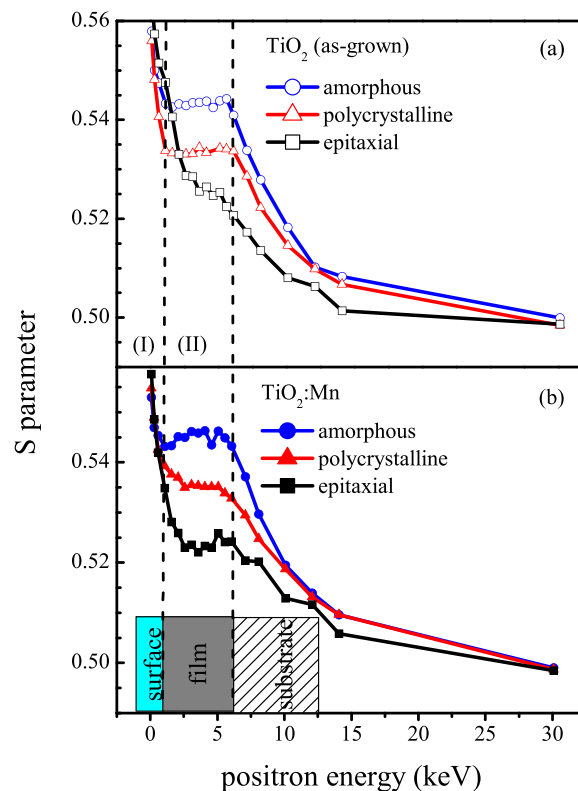

FIG. 1. S parameter depth profiles of as-grown (a) and Mn$^+$-implanted (b) TiO_2 structures. Dashed lines are present to guide the eyes and the energy range between them roughly corresponds to film body. A schematic sketch of the positron energy-depth profile through a thin film sample is given at the bottom of the figure.
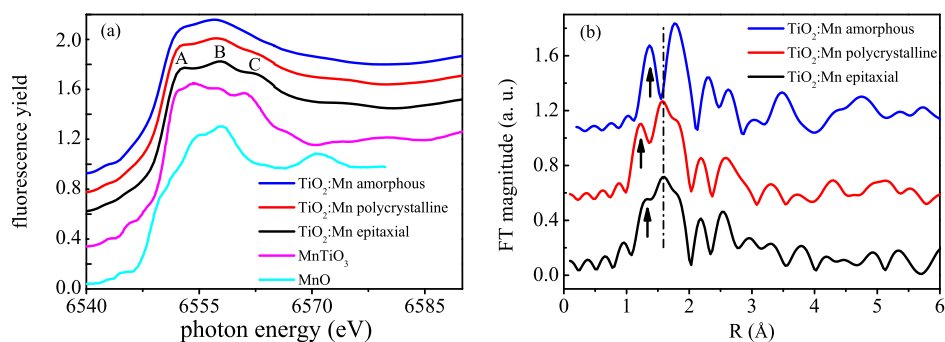
FIG. 2. (a) Mn K-edge XANES spectra of Mn^+-implanted TiO_2 structures along with reference spectra of MnO[16] and MnTiO$_3$[17] (reference spectra shifted vertically for clarity by considering the energy calibration of experimental setup). Data were obtained in grazing incidence geometry at 1° to enhance the Mn fluorescence signal. A, B, and C are given in order to guide the eyes and represent three distinct features, which show differences for each microstructure type. (b) Fourier transform of k^3-weighted extended XANES spectra of the experimental data. (The FT are not corrected with a phase shift.) The dotted-dashed line as well as arrows is present to guide the eyes.

implanted Mn atoms are in (II) oxidation state. In spite of an octahedral oxide coordination of Mn in both MnO and MnTiO$_3$, the difference in the local Mn-O coordination depends on the distortion of the octahedron, which can also be probed and distinguished by XANES measurements.[18,19] The XANES spectra of the three TiO$_2$:Mn films are dominated by three common features A, B, and C (Fig. 2(a)). These features are most pronounced in the case of the epitaxial film and resemble the MnTiO$_3$ spectrum. With increasing structural disorder from epitaxial to polycrystalline TiO$_2$, the features A–C tend to broaden. In particular, feature C, which appears as a weak shoulder in the polycrystalline film, vanishes in the case of the amorphous TiO$_2$:Mn, i.e., its presence reflects higher microstructural order. The Fourier transforms (FT) of the $k^3\chi(k)$ weighted Mn K-edge spectra of the Mn^+-implanted TiO$_2$ films are depicted in Fig. 2(b). The most intense FT peak of the epitaxial film was found at the same position for Ti in anatase structure.[20] Correspondingly, peak at around 1.60 Å (marked with a dashed-dotted line) is related to the Mn-O distance in the octahedron. For the amorphous film, this peak is shifted, which suggests a different Mn-O distance as compared to the epitaxial and the polycrystalline films. On the other hand, this peak contains a weak shoulder (shown by arrows) at around 1.3 Å for the epitaxial film. This shoulder becomes more pronounced for the polycrystalline film and eventually for the amorphous film it becomes almost an independent peak separated from the main peak. This situation seems to reflect different distortions of the octahedron.[21] Backscattering amplitudes and sizes of Mn and Ti atoms are slightly different, so if both of

these atoms occupy the equivalent positions in the same matrix, the corresponding EXAFS signal will be disturbed and the most intense line of the FT could broaden. As a consequence, for the amorphous film, Mn atoms show different coordination geometry as compared to the epitaxial film. The similarities between the spectra obtained from the epitaxial film and Mn environment in MnTiO$_3$ and Ti environment in the anatase TiO$_2$ imply that most of the implanted Mn atoms within the epitaxial film reside in Ti lattice sites. For the polycrystalline film, due to a pronounced shoulder at 1.3 Å as compared to the epitaxial film, the Mn atoms appear to have two types of oxide coordination geometries, i.e., only a partial incorporation of Mn by substitution of Ti must be assumed.

The temperature dependent magnetometry results for the Mn^+-implanted TiO$_2$ structures are shown in Figure 3. It is worth to note that prior to implantation, all of the as-grown TiO$_2$ films showed only diamagnetic response. The Mn^+-implanted amorphous film exhibits a splitting between ZFC and FC curves and an antiferromagnetic-like transition at around 110 K (Fig. 3). This value is in agreement with the Néel temperature of MnO,[22,23] supporting the secondary phase-like coordination geometry of Mn in amorphous TiO$_2$ found from XANES measurements. Mn^+-implanted polycrystalline film shows a ferromagnetic behavior with a T_C of around 230 K. At low temperatures (T ≤ 25 K), the magnetization of the polycrystalline film shows a tendency to decrease (Fig. 3), suggesting the existence of antiferromagnetic interactions. The saturation magnetization of polycrystalline TiO$_2$:Mn was found to be around 0.85μ_B/Mn at 20 K
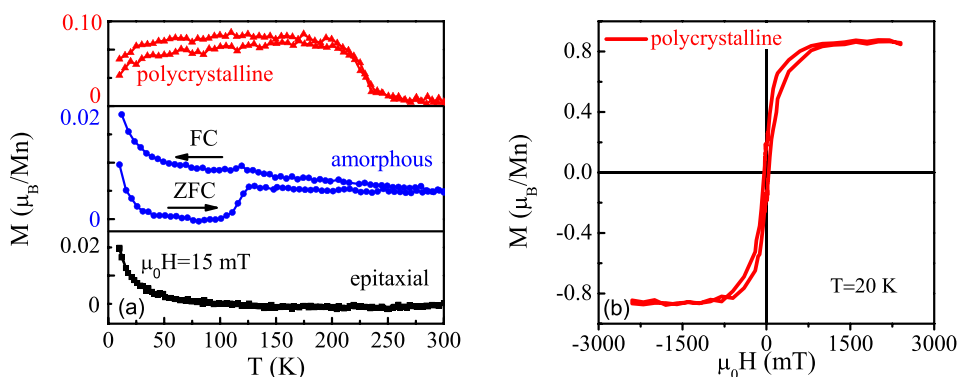

FIG. 3. (a) In-plane thermal scans of the magnetization of Mn^+-implanted TiO$_2$ films with different as-grown microstructures. (b) In-plane magnetic field dependent magnetization curve of Mn^+-implanted polycrystalline film at 20 K. For all of the measurements, diamagnetic contribution of the substrate was subtracted. Magnetic moment per Mn atom values were calculated by taking into account of total number of the implanted Mn atoms, independent of lattice-host incorporation.

(Fig. 3). These two contributions to magnetic properties of the polycrystalline film support the presence of two different local environments of Mn, as indicated by XANES. By comparison to the amorphous film, the antiferromagnetic-like negative contribution is attributed to a Mn related secondary phase, whereas the FM is due to the presence of Mn_{Ti} substitutional sites. On the other hand, although most of the Mn atoms in the epitaxial film substitutes for Ti, this sample shows no signs of FM but, a well defined weak paramagnetic behavior. Recently, it was reported that the FM in transition metal doped anatase TiO_2 appears above a certain carrier concentration $(\sim 1.8 \times 10^{19}\,cm^{-3})$.[24] This is comparable to the value measured in polycrystalline TiO_2:Mn, whereas the carrier concentration in the epitaxial sample is below. This may explain the absence of ferromagnetic interactions in the epitaxial TiO_2:Mn sample investigated in the present work. On the other hand, absence of AHE in polycrystalline anatase TiO_2:Mn is attributed to low carrier concentration.[25] Furthermore, compared to a previous study on 5 at. % Mn^+-implanted rutile TiO_2 single crystals,[26] the ferromagnetic behavior found for the polycrystalline film shows differences in saturation and thermal magnetization behavior. The extrapolated Curie temperature in Ref. 26 was found to be around room temperature, and the highest saturation magnetization is reported to be around $0.4\mu_B$. These differences must be attributed to the use of rutile TiO_2 in contrast to anatase TiO_2 in the present study. Our results also differ significantly from pure defect-induced FM in two main points. First, it is observed that the polycrystalline TiO_2:Mn is ferromagnetic with a Curie temperature at around 230 K, while almost all of the studies on the defect-induced FM report that ferromagnetic order exist above room temperature.[27] In addition, we find that the observed FM is correlated to the dopant type. In a recent study, we have investigated 5 at. % Co^+ implantation into the same type of polycrystalline anatase TiO_2 films under equivalent conditions.[11] In contrast to Mn^+ implantation, Co^+ implantation leads to paramagnetism independent of the crystalline structure of the as-grown films.

In summary, we have prepared TiO_2:Mn (5 at. %) with amorphous, polycrystalline anatase and epitaxial anatase structure. The initial microstructure, characterized by open-volume defect concentration and crystallographic order, strongly affects the magnetic properties upon Mn^+ implantation. The FM, observed in the Mn^+-implanted polycrystalline film, is attributed to the presence of a high carrier concentration together with a sufficient amount of defects, which facilitate ferromagnetic coupling. On the other hand, paramagnetic behavior has been observed in the case of the epitaxial TiO_2:Mn film, which showed the lowest defect concentration and lower carrier density as compared to the polycrystalline film. The magnetic properties of the amorphous film are attributed to the secondary phase formation. The observed dopant type, carrier, and defect concentration dependent ferromagnetic behavior points towards an intrinsic mechanism for ferromagnetic order in Mn^+-implanted polycrystalline anatase TiO_2 film, and it is generally consistent with a bound magnetic polaron description.[28,29] Consequently, our results suggest that polycrystalline anatase TiO_2 is an excellent candidate structure for DMO applications.

[1]Y. Matsumoto, M. Murakami, T. Shono, T. Hasegawa, T. Fukumura, M. Kawasaki, P. Ahmet, T. Chikow, S. Koshibara, and H. Koinuma, Science **291**, 854 (2001).

[2]W. Prellier, A. Fouchet, and B. Mercey, J. Phys. Condens. Matter **15**, R1583 (2003).

[3]J. B. Goodenough, *Magnetism and the Chemical Bond* (Interscience, New York, 1963).

[4]D. W. Abraham, M. M. Frank, and S. Guha, Appl. Phys. Lett. **87**, 252502 (2005).

[5]N. Akdogan, A. Nefedov, R. I. Khaibullin, A. Westphalen, L. R. Tagirov, B. Aktas, and H. Zabel, J. Magn. Magn. Mater. **300**, e4 (2006).

[6]T. Tietze, P. Audehm, Y. C. Chen, G. Shutz, B. B. Straumal, S. G. Protasova, A. A. Mazilkin, P. B. Straumal, T. Prokscha, H. Luetkens, Z. Salman, A. Suter, B. Baretzky, K. Fink, W. Wenzel, D. Danilov, and E. Goering, Sci. Rep. **5**, 8871 (2015).

[7]J. M. D. Coey, P. Stamenov, R. D. Gunning, M. Venkatesan, and K. Paul, New J. Phys. **12**, 053025 (2010).

[8]Y. B. Nian, J. Strozier, N. J. Wu, X. Chen, and A. Ignatiev, Phys. Rev. Lett. **98**, 146403 (2007).

[9]J. F. Ziegler, M. D. Ziegler, and J. P. Biersack, Nucl. Inst. Methods Phys. Res. B **268**, 1818 (2010).

[10]The ion energies of 190 keV, 100 keV, 70 keV, 50 keV, and 30 keV applied sequentially, while the ion fluences of 42×10^{15} at./cm³, 11.5×10^{15} at./cm³, 3.75×10^{15} at./cm³, 4.75×10^{15} at./cm³, and 3.75×10^{15} at./cm³ have been employed from the highest energy to the lowest, respectively.

[11]O. Yildirim, S. Cornelius, A. Smekhova, G. Zukov, E. A. Ganshina, A. Granovsky, R. Huebner, C. Baehtz, and K. Potzger, J. Appl. Phys. **117**, 183901 (2015).

[12]N. Akdogan, A. Nefedov, K. Westerholt, H. Zabel, H.-W. Becker, C. Somsen, R. I. Khaibullin, and L. R. Tagirov, J. Phys. D: Appl. Phys. **41**, 165001 (2008).

[13]W. Anwand, G. Brauer, M. Butterling, H. R. Kissener, and A. Wagner, Defect Diffus. Forum **331**, 25 (2012).

[14]M. P. Petkov, M. H. Weber, K. Lynn, K. P. Rodbell, and S. A. Cohen, Appl. Phys. Lett. **74**, 2146 (1999).

[15]Y. Furubayashi, T. Hitosugi, Y. Yamamoto, K. Inaba, G. Kinoda, Y. Hirose, T. Shimada, and T. Hasegawa, Appl. Phys. Lett. **86**, 252101 (2005).

[16]K.-W. Nam, M. G. Kim, and K.-B. Kim, J. Phys. Chem. C **111**, 749 (2007).

[17]M. Valant, T. Kolodiazhnyi, I. Arcon, F. Aguesse, A.-K. Axelsson, and N. M. Alford, Adv. Funct. Mater. **22**, 2114 (2012).

[18]L. Zhang, J. Li, Y. Du, J. Wang, X. Wei, J. Zhou, J. Cheng, W. Chu, Z. Jiang, Y. Huang, C. Yan, S. Zahng, and Z. Wu, New J. Phys. **14**, 013033 (2012).

[19]S. W. Chen, P. A. Lin, H. T. Jeng, S. W. Fu, J. M. Lee, J. F. Lee, C. W. Pao, H. Ishii, K. D. Tsuei, N. Hiraoka, D. P. Chen, S. X. Dou, X. L. Wang, K. T. Lu, and J. M. Chen, Appl. Phys. Lett. **104**, 082104 (2014).

[20]G. Vlaic, J. C. J. Bart, W. Cavigiolo, S. Mobilio, and G. Navarra, Z. Naturforsch. **86a**, 1192 (1981), available at http://zfn.mpdl.mpg.de/data/Reihe_A/36/ZNA-1981-36a-1192.pdf.

[21]T. Nedoseykina, M. G. Kim, S.-A. Park, H.-S. Kim, S.-B. Kim, J. Cho, and Y. Lee, Electrochem. Acta **55**, 8876 (2010).

[22]D. P. Shoemke, M. Grossman, and R. Seshadri, J. Phys.: Condens. Matter **20**, 195219 (2008).

[23]Z. Ge, W. L. Lim, S. Shen, Y. Y. Zhou, X. Liu, J. K. Furdyna, and M. Dobrowolska, Phys. Rev. B **75**, 014407 (2007).

[24]T. S. Krasienapibal, S. Inoue, T. Fukumura, and T. Hasegawa, Appl. Phys. Lett. **106**, 202402 (2015).

[25]J. S. Higgins, S. R. Shinde, S. B. Ogale, T. Venkatesan, and R. L. Greene, Phys. Rev. B **69**, 073201 (2004).

[26]D. Menzel, I. Jursic, J. Schoenes, F. Iacomi, and D. Cacaina, Phys. Status Solidi C **3**, 4119 (2006).

[27]P. Esquinazi, W. Hergert, D. Spemann, A. Setzer, and A. Ernst, IEEE Trans. Magn. **49**(8), 4668 (2013).

[28]A. Kaminski and S. DasSarma, Phys. Rev. Lett. **88**, 247202 (2002).

[29]H. Chou, C. P. Lin, J. C. A. Huang, and H. S. Hsu, Phys. Rev. B **77**, 245210 (2008).